Time, temperature and concentration resolved Yb3+ luminescence study in co-sputtered Cu2-xGaxS2 (0.1 < x < 1.6) thin films with a Cu–Ga composition gradient

Derksen, Max; Bergkamp, Sem; Kohnstamm, Olivia; van der Kolk, Erik

DOI
10.1016/j.optmat.2024.116220

Publication date
2024

Document Version
Final published version

Published in
Optical Materials

Optical Materials 157 (2024) 116220

Contents lists available at ScienceDirect

Optical Materials

journal homepage: www.elsevier.com/locate/optmat

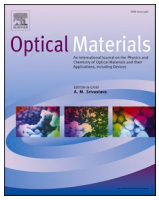

Research Article

Time, temperature and concentration resolved Yb^{3+} luminescence study in co-sputtered $Cu_{2-x}Ga_xS_2$ ($0.1 < x < 1.6$) thin films with a Cu–Ga composition gradient

Max Derksen *, Sem Bergkamp, Olivia Kohnstamm, Erik van der Kolk

Delft University of Technology, Netherlands

ARTICLE INFO

Keywords:
Thin film luminescent solar concentrator
Combinatorial sputtering
$CuGaS_2$:Yb^{3+} photoluminescence
Host sensitized emission
Charge trapping mediated energy transfer

ABSTRACT

The broad class of Cu(Al,Ga,In) $(S,Se,Te)_2$ solar absorber materials when doped with Yb^{3+} are interesting for thin film based luminescent solar concentrator (LSC's) application. In this work the strong and broad absorption properties of co-sputtered $CuGaS_2$ (CGS) thin films combined with the luminescent properties of Yb are reported. Energy-dispersive x-ray spectroscopy (EDS), x-ray diffraction, transmission, excitation, and temperature dependent emission as well as radiative lifetime measurements are performed on thin films with varying Cu:Ga ratios and Yb^{3+} concentrations. It is found that Yb^{3+} emission can be broadly sensitized by the host in the range of 200–600 nm. A lower Cu:Ga ratio, crystallinity and post annealing in air provides a positive impact on the sensitization of Yb^{3+} emission. The temperature dependent time integrated decay curves show a clear thermal energy barrier of about 0.2 eV. Because the exponential tail, with a lifetime of 110 μs, is constant with temperature, we conclude that the barrier is connected to the thermal release of electrons trapped at the Yb^{2+} ground state. The low energy transfer efficiency from the host to the Yb dopant is attributed to efficient non-radiative electron-hole pair recombination. The prospects and design criteria of Cu(Al,Ga,In) $(S,Se,Te)_2$ solar absorber materials for LSC applications is the further subject of the discussion.

1. Introduction

1.1. CIGS and LSCs

Copper Gallium/Indium Selenide/Sulfide (CIGS) type thin film solar cells gained significant interest since their debut in 1976 [1]. The versatility, strong absorption coefficient and lower manufacturing cost compared to traditional Si solar cells was the driving force behind their continued development. From the inception of the CIGS to now, the energy conversion efficiencies improved from a meager 4.5 % to an impressive 22.3 % [1,2]. Despite this significant improvement, the thin film based solar cells (including CIGS, CdTe and amorphous Si-based) market share has been steadily decreasing from 17 % in 2009 to 7–8% in 2014. Several factors contribute to this decline including the reduced cost in conventional crystalline Si solar cells, the reluctance to work with known toxic elements such as Cd and relatively scarce metals such as In [3].

Luminescent solar concentrators (LSCs) share a similar story to that of the CIGS solar cells. First conceptualized in the same year as the CIGS thin film solar cell and vastly improved power conversion efficiencies over the years [4,5]. The basic operating principle of an LSC is to absorb incoming sunlight using a sheet of glass or polymer doped with luminescent centers. The absorbed sunlight is re-emitted at longer wavelengths by the luminescent centers and is wave-guided to the edges by the glass/polymer. Solar cells installed at the edge of the wave-guide can harvest and convert the emitted energy to useable electricity, thereby creating an electricity generating window. Similarly to the CIGS thin films solar cells, LSC's can also be made as a thin film and share similar benefits to CIGS. Rapid implementation, up-scalable and lower manufacturing costs.

A key challenge for thin film based LSC's is the limited thickness available for absorption. What's more is that in order to achieve appreciable power conversion efficiencies of more than 1 % requires absorption of both UV and the visible part of the spectrum [6]. This leads to other challenges such as unwanted colorization of the window. To mitigate the unwanted colorization of a window requires that the thin

* Corresponding author.
E-mail addresses: m.derksen-2@tudelft.nl (M. Derksen), sembergkamp@gmail.com (S. Bergkamp), oliviakohnstamm@gmail.com (O. Kohnstamm), E.vanderKolk@tudelft.nl (E. van der Kolk).

https://doi.org/10.1016/j.optmat.2024.116220
Received 5 June 2024; Received in revised form 27 September 2024; Accepted 3 October 2024
Available online 5 October 2024

film absorbs across the entire visible spectrum. Luminescent centers such as the trivalent rare-earths Nd^{3+} and Yb^{3+} have narrow and weak absorption properties due to their forbidden 4f-4f transitions and are therefore unsuitable for LSC applications without a sensitizer. The selenide based CIGS however, with its broad and narrow-bandgap transition (absorption <800 nm) and high absorption coefficient (>1 * 10^5 cm^{-1}), is able to absorb nearly all of the UV and visible part of the solar spectrum in just 1 μm [7]. The absorption properties of the CIGS type thin film material, combined with the luminescent properties of trivalent rare-earths would make an ideal candidate for a thin film LSC. The requirement is that the CIGS host can efficiently sensitize the trivalent rare-earth. Numerous work has been done on semiconductor quantum dots doped with trivalent lanthanides (Ln^{3+}) [8–10]. To our knowledge, no work has been done on doping Ln^{3+} in CIGS type hosts in thin films for LSC applications. In this work we hypothesize an energy transfer mechanism between the CIGS host and Ln^{3+} doping and discuss its validity through experimental photoluminescence results on sputtered $CuGaS_2$:Yb^{3+} thin films.

1.2. Energy transfer mechanism

Two well-known energy transfer mechanisms are presented by Förster (dipole-dipole interaction) and Dexter (exchange interaction) [11,12]. Both of these interactions are strongly dependent on spectral overlap between a sensitizer and activator. Mukherjee et al. provide an elaborate discussion on why these two mechanisms are likely to be negligible for the sensitization of Tb^{3+} and Eu^{3+} in ZnS nanoparticles [13]. Instead, they describe a mechanism that involves the Ln^{3+} acting as either an electron or hole trap followed by a recombination event at the lanthanide site leaving the Ln^{3+} in an excited state.

The *charge trapping mediated Ln^{3+} emission sensitization mechanism*, as they call it [14,15], can be modelled using the vacuum referred binding energy (VRBE) diagrams developed by P. Dorenbos [16–21]. These diagrams relate position of the valence and conduction band of the host to the ground and excited states of all divalent and trivalent lanthanides and thereby possibilities for electron and hole trapping. In Fig. 1 such a diagram is presented to visualize the charge trapping mediated Ln^{3+} emission sensitization mechanism. The steps of the sensitization mechanism are described by the arrows and their corresponding equations listed below. Fig. 1 serves as a conceptual diagram and therefore does not provide absolute energy values. More examples of such a diagram of ZnX and CdX (X = S, Se, Te), but with absolute energy values, can be found in the work by Mukherjee et al. [13] First an electron-hole pair is generated after the absorption of a photon with enough energy to cross the band-gap as shown by arrow 1, Fig. 1. If the Ln^{3+} dopant ground state lies above the hosts valence band, then the dopant can act as a trap for a hole.

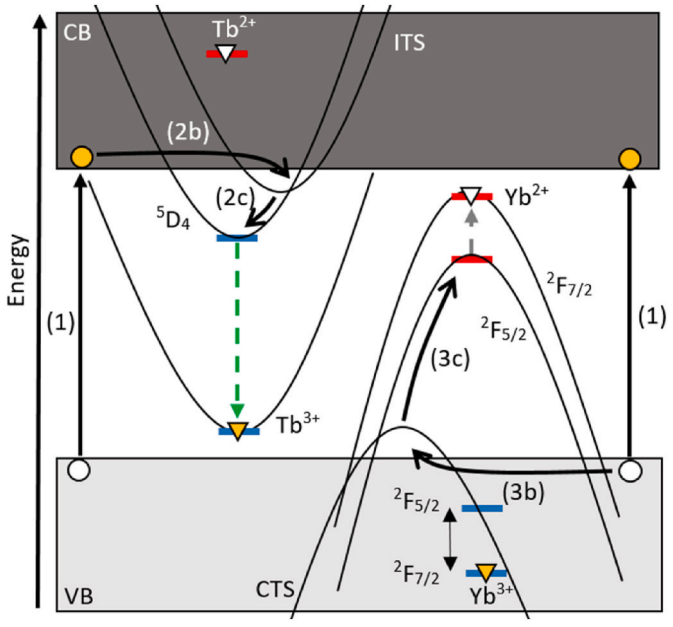

Fig. 1. A vacuum referred binding energy (VRBE) scheme along with configurational coordinate parabolas showing the proposed energy transfer mechanism. (1) generation of electron hole pair after photon absorption. (2b, 3b) electron or hole trapped by impurity-trapped state or charge transfer state respectively. (2c, 3c) electron or hole recombines with hole or electron respectively and leaves Ln^{3+} in the excited state.

$$Ln^{3+} + h^{+} \rightarrow \left[Ln^{3+} + h^{+}\right] \rightarrow Ln^{4+}, \tag{2a}$$

where the notation $\left[Ln^{3+} + h^{+}\right]$ indicates a charge transfer (CT) state. The possibility of hole trapping is however limited to the ions Ce^{3+}, Pr^{3+} and Tb^{3+}. The other lanthanides have their ground state below the valence band maximum. The coulomb interaction will localize an electron near the trapped hole and subsequent recombination can lead to Ln^{3+} in the excited state.

$$Ln^{4+} + e^{-} \rightarrow Ln^{3+*} \tag{2b}$$

The alternative host-to-Ln^{3+} ion energy transfer route is electron trapping.

$$Ln^{3+} + e^{-} \rightarrow \left[Ln^{3+} + e^{-}\right] \rightarrow Ln^{2+} \tag{3a}$$

Followed by hole trapping at the dopant site and again creation of the excited Ln^{3+}

$$Ln^{2+} + h^{+} \rightarrow Ln^{3+*} \tag{3b}$$

For electron trapping to happen it requires that the Ln^{2+} ground state lies below the conduction band of the host which is most likely the case for ions like Eu^{2+}, Sm^{2+}, Yb^{2+} and Tm^{2+}. It is a misconception that excited 4f levels of Ln^{3+} ions (given by a Dieke diagram) lying below the conduction band can be electron traps. These excited states are electron donor states, not acceptor states. Only by first trapping the hole, creating Ln^{4+}, will the Ln^{3+} ground and excited states act as electron acceptor states or electron traps.

It is generally more intuitive, due to common convention, to follow the path of electrons than holes. In case of an electron trapping process shown in on the left in Fig. 1 (2b and 2c), it is straightforward to visualize an electron moving through the conduction band to the first available energy level of Tb^{3+} below the conduction band (Tb^{3+} is shown as an example). Note that the electron can only be trapped by Tb^{4+} which is formed after the hole has been trapped by the Tb^{3+} ion. When the electron recombines with the Tb^{4+} ion it leaves a Tb^{3+} ion in one of its excited states below the CB as indicated in Fig. 1 and equation (2c). It is possible that the electron is first trapped in a 5d state of the Ln^{3+} ion or in a so-called Ln-trapped exciton state or impurity-trapped state $\left[Ln^{4+} + e^{-}\right]$ that can be visualized by the shifted parabola labelled ITS (shown by 2b, Fig. 1).

However, when an electron is trapped first by a Ln^{3+} ion, thereby creating Ln^{2+}, it is difficult to visualize how one ends up with Ln^{3+} in the excited state after the hole recombines with Ln^{2+}. P. Dorenbos provided a useful insight in 2018 through what he calls the 'hole picture' [22]. The hole picture provides a convenient way to follow the path of the hole and is sometimes used in semiconductor physics [23]. In a typical energy diagram, like Fig. 1, the electron moves up as it gains energy and moves down as it relaxes. Contrarily, holes move up as they relax and down as they are excited. The excited Ln^{3+} states can be visualized by flipping the Dieke diagram upside down and placed with the Ln^{3+} ground state at the Ln^{2+} ground state. Traditional configurational coordinate diagrams can again be used to represent the well-known charge transfer (CT) states (like that for Eu^{3+} or Yb^{3+}) in which a hole is trapped at the anion states coordinating the Ln^{2+} ion. Taken together we have a clearer

picture of the sensitization of a Yb^{3+} ions mediated by a charge trapping mechanism. After Yb^{2+} is formed there is a CT state available for the hole to relax to, situated above the valence band (shown by 3b). From this CT state it can relax further to the excited Yb^{3+} state (3c). Yb, the subject of this paper, is used as an example of this mechanism. A similar process would be true for Eu.

The efficiency of the sensitization of the Ln^{3+} through this mechanism will be dependent on various parameters. First of all the electron and hole must have ample time to be trapped by the dopant. Therefore, the lifetime and mobility of the exciton must be sufficient to sensitize the Ln^{3+} dopant. What's more, considering the Yb^{3+} case, the Yb^{2+} ground state must not be situated too close to the conduction band as ionization can then be thermally activated where the electron escapes through the conduction band. Another quenching route can happen when the hole in the CTS can relax directly to the ground state, rather than to the excited state. Taken together, the position of the valence and conduction band relative to the Ln^{3+} dopant, the position of the CTS, and the intrinsic exciton properties of the host material are key parameters for the efficiency of the energy transfer in this mechanism.

It has been shown that these parameters can be tuned in $CuGaS_2$ by varying the Cu:Ga content [24]. Combinatorial sputtering allows to create thin films with a compositional gradient. With this method a $CuGaS_2$ thin film doped with Yb^{3+} can be created that has a varying Cu:Ga ratio as a function of position on the film. Therefore, in the first part of this work a photoluminescence study on a composition gradient $CuGaS_2$:Yb^{3+} thin film with varying a Cu:Ga content and Yb concentration is presented. The second part is a more detailed study, including x-ray diffraction, excitation spectra and temperature and time dependent luminescence is presented comparing three homogenous thin films with a Cu:Ga ratio of 0.95:1, 0.79:1 and 0.68:1. Finally a copy of the most efficient sample is post annealed in air and reinvestigated. More details on the synthesis of these films can be found in the experimental details section.

2. Experimental details

2.1. Fabrication of thin films

A total of 4 samples were deposited on a 50x50 × 1 mm^3 fused silica substrate using an AJA ATC Orion 5 magnetron sputtering system. Sputtering was done in an argon atmosphere from three targets: $CuGaS_2$ (99.99 %), Cu (99.9 %), Yb (99.99 %) (Demaco). It was found that sputtering from a single $CuGaS_2$ target resulted in a significant deviation from a 1:1 Cu:Ga ratio. Therefore, a Cu target was co-sputtered to compensate. It should be noted that others have done a study on the sputtering of $Cu(InGa)Se_2$ from a single target [25], however that is not the subject of this paper. The Cu target is connected to a pulsed direct current (DC) power supply, whilst the $CuGaS_2$ and Yb targets are connected to radio-frequency (RF) power supplies. Prior to deposition the sputter chamber is evacuated to a base pressure in the order of 0.1 mPa. The working pressure during sputtering is 0.4 Pa with an argon gas flow of 15 sccm. Sputtering parameters used per sample can be seen in Table 1. The final three samples, S2, S3 and S4 were sputtered using a fresh $CuGaS_2$ target. For this reason, there is a significant power difference on the $CuGaS_2$ targets between S1 and the others as the deposition rate was different for the two targets. The working distance between target and substrate is 10 cm. The three targets are at right angles from one another, where each target is aligned so that the highest deposition rate is the located at edge of the substrate, in a sputter up configuration. In order to achieve doping concentrations (1 %) of Yb a mask with holes is installed above the target to reduce deposition rates by roughly 90 %. Similarly for Cu a mask was installed to reduce the deposition rate by roughly 60 %. The substrate is heated at 250 °C during deposition. For S1 the substrate is not rotated to obtain a compositional gradient. The orientation of the film and the compositional gradient can be seen in Fig. 2b. The other films, S2, S3 and S4, are homogenous obtained by rotating the target with different Cu:Ga ratios obtained by having the Cu target at different powers. A schematic of the sputter coater can be seen in Fig. 2a. After deposition, each sample was post annealed in vacuum at 350 °C, according to an optimization study done by another group [26]. In an attempt to optimize the Yb^{3+} intensity, one of the four pieces of the most emitting sample, S4, was post annealed in air for half an hour at 400°.

Table 1
Sputter deposition conditions of the samples.

ID	Gradient	$CuGaS_2$/Cu/Yb Power (W)	Deposition Time (s)
S1	Yes	110/30/15	10000
S2	No	180/40/15	7500
S3	No	180/20/15	8500
S4	No	180/0/10	11500

2.2. Characterization of thin films

Energy-dispersive X-ray spectroscopy (EDS/EDX) measurements were done for 60 s using the JEOL JSM-IT100 EDX/SEM electron microscope at ×1000 magnification with an acceleration voltage of 12 kV, probe current of 60 % and in a low vacuum pressure of 35 Pa. For the homogenous films a total of 5 measurements were done on various positions on the film.

X-ray diffraction (XRD) measurements were performed with a fixed slit width of ½ cm for half an hour using the PANalytical X'pert Pro MPD diffractometer. The equipment consists of a Cu Kα (1.54056 Å) anode which is operating at 45 kV and 40 mA.

Photoluminescence emission, excitation and lifetime measurements were done with an optical parametric oscillator OPO EKSPLA/NT230 laser as excitation source with a pulse duration of 3–6 ns FWHM. Excitation wavelength is tunable between 193 and 2600 nm. A beam splitter is used to re-direct part of the laser to the sample, whilst the transmitted part is read out by Thorlabs thermal power meter to correct for the power of the laser in excitation measurement mode. Appropriate cut-off filters were used to remove the laser observed in second order from emission measurements. Luminescence is collected by an optical fiber connected to an Ocean Optics QE Pro (350–1100 nm) spectrometer for emission/excitation measurements. For lifetime measurements the optical fiber is connected to a Hamamatsu H10330A-75 (950–1700 sensitivity) photomultiplier tube both operating at 800V which is subsequently read out by a CAEN DT5724 digitizer after a trigger pulse from the EKSPLA laser. Transmission measurements were performed using an Avantes DH-S lamp which is a combination of a deuterium and a halogen lamp. The light is transported by an optical fiber and collimated to a spot (2 mm diameter) and subsequently collected by a focusing mirror and then transported through another optical fiber connected to and read out by the Ocean Optics QE65 Pro (230–900 nm).

All measurements on the gradient film were performed by placing

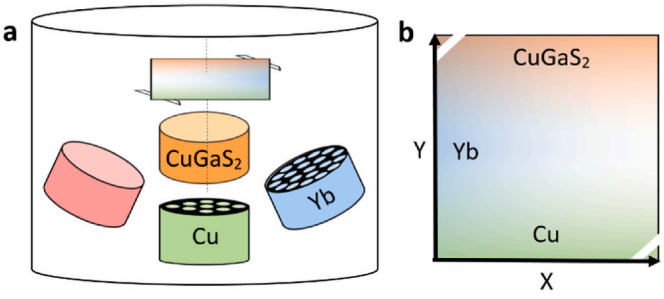

Fig. 2. a: Schematic of the sputter coater with the orientation of each source. b: schematic of the gradient film (film side on top) where the colours represent a concentration gradient of the corresponding target.

the sample on two translation stages at right angles with precise position read-out in order to analyze the sample on a 17x17 grid. EDS measurements for the gradient film are made along a vertical line with varying Cu:Ga ratios or a horizontal line for constant Cu:Ga ratios, but varying Yb concentration. This allows to correlate the compositions of the film directly to the film material properties. Further details on this method can be found in previous work [27].

Lastly, quantum efficiency measurements presented in this work is found using an integrating sphere with two optical fiber connectors, an LED at 375 nm with a full width at half maxima of 25 nm and the Ocean Optics QE Pro (350–1100 nm) spectrometer. A couple of optical fibres are used to couple the LED light into the integrating sphere whilst another is connected to the spectrometer. First a measurement is done with a substrate inside the integrating sphere. Then a measurement is taken with a substrate that has a thin film deposited. The difference in the LED intensity between the two measurements is taken as the absorption, whilst the difference in Yb^{3+} emission (around 970 nm) is used as the emission intensity. Emission counts divided by absorption counts is used to estimate the quantum efficiency of the sample.

3. Results & discussion

3.1. Gradient thin films

An image of the S1 film is shown in Fig. 3. The orientation of the film is the same as depicted in Fig. 2b. The color of the film changes from a dark brown to a light yellow from the bottom (Cu rich) to the top (Cu poor). EDS measurements along the center vertical, indicated by circular white markers in Fig. 3, show that the Cu/Ga ratio ranges from 1.91 to 0.40 from bottom to top. The S/(Cu + Ga) ratio changes along this vertical between 0.84 and 1.10. The EDS and other results are summarized in Table 2. In Fig. 4b, XRD measurements done on Y = 5, 25 and 45 mm are presented and show that only the $CuGaS_2$ phase is present (JCPDS#25–0279). The Yb content ranged between 0.33 and 0.75 % with an average of 0.53 %. There was no clear gradient of the Yb content along the vertical like for the Cu/Ga and S/(Cu + Ga) ratios, which is to be expected as the Yb source is at a right angle of the vertical. The Yb content is expressed as the percentage of all cations (Yb, Cu and Ga).

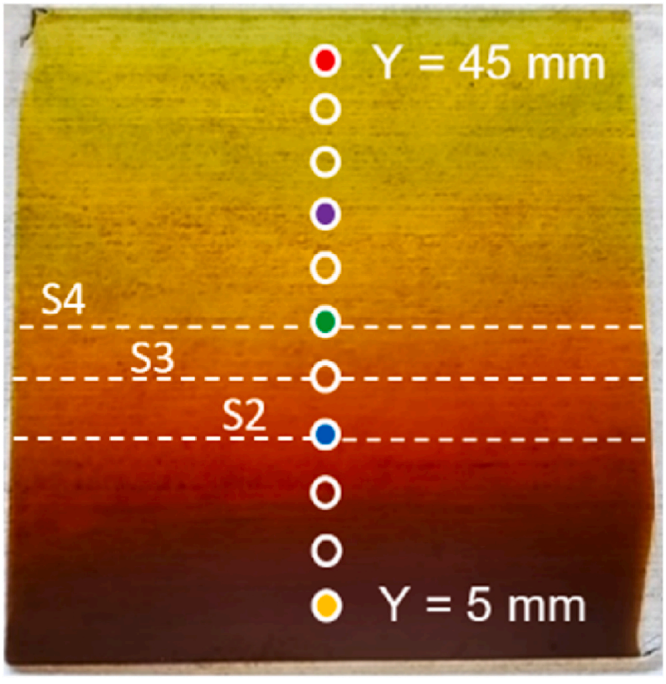

Fig. 3. Photograph of S1 with white circular markers to indicate where EDS measurements were done which are presented in Table 2. Transmission, XRD and (time-resolved) emission measurements (presented in Fig. 4a–b, 6 and 7) were recorded at the colored markers. The three white dashed lines indicate the position on the film where the Cu:Ga ratio represents that of the three homogenous films presented later.

In Fig. 4 the position dependent transmission and XRD measurements taken at the colored markers in Fig. 3 are presented. As the photo in Fig. 3 suggests, the absorption edge is blue shifted towards the top of the sample (Cu poor and S rich). A thin film interference pattern is observed at longer wavelengths (>600 nm). Fitting the interference fringes with the Swanepoel method allows to estimate the film thickness and refractive index (defined at 589 nm) [28]. However, towards the bottom of the film (Y = 5 mm) the thin film interference is not observed, which does not allow for proper fitting of the fringes. The thickness increased from 630 nm to 950 nm and the refractive index decreased from 2.52 to 2.30 going from Y = 17 mm to Y = 45 mm. All fits had an R-square value higher than 0.99. The increase in thickness towards the top is expected due to the higher deposition rate of the $CuGaS_2$ target at the top. The absorption edge shift can be attributed to the widening of the $CuGaS_2$ bandgap due to a deficiency in Cu, which is thought to be caused by a lowering of the valence band according to a previous study [24]. The XRD measurements shown in Fig. 4b are taken at positions Y = 5, 25 and 45 mm and are plotted on a logarithmic scale. All measurements have a broad peak at 22° originating from the amorphous fused silica substrate. A single common peak is observed at 28° related to the $CuGaS_2$ crystal structure. The peak decreases in intensity towards the top of the film, where the film becomes more deficient in Cu. Typically XRD of $CuGaS_2$ has 7 peaks between 20 and 60°, with the main peaks at 28, 48 and 57° (JCPDS#25–0279). However, thin films can be textured, which is a result of a preferred crystallite growth orientation during deposition. The bottom of the film (Y = 5 mm, in yellow) has a second observed peak at 48° also related to the $CuGaS_2$ structure. Other phases such as Cu, CuS, CuS2, CuO, Cu_2O or Ga_2S_3 where not observed. The gradient film can best be interpreted as an amorphous defect rich $Cu_xGa_yS_2$ film with a varying fraction of $CuGaS_2$ crystallites.

The transmission measurements presented in Fig. 4, along with the retrieved thickness using the Swanepoel method, can be used to estimate a band-gap value of our thin film using the Tauc method [29]. To apply the Tauc method a direct band-gap is assumed throughout the thin film. In Fig. 5 the absorption coefficient, α (cm^{-1}), is plotted against photon energy (eV) at the same positions as shown by the corresponding colored markers in Fig. 3. As per the Tauc method, the first linear region is extrapolated to intersect with the x-axis (shown by the dotted line). The value of the intersect is an estimation of the local band-gap of the material. The position-dependent band-gap values are summarized in Table 2. Similar difficulties as with the Swanepoel method prevent a band-gap estimation on the bottom side of the film.

The Yb^{3+} emission intensity (λ_{exc} = 375 nm) has also been measured at the same points as the transmission measurements, shown in Fig. 6. The well-known $^2F_{5/2}$ -> $^2F_{7/2}$ 4f-4f transition maximum of Yb^{3+} is observed at 980 nm. The inset of Fig. 6 shows heat map of the Yb^{3+} intensity across the entire film. The Yb^{3+} intensity heat map has a similar shape as that of the photo in Fig. 3. Comparing Figs. 5 and 6 it is clear that an increase in the band gap results in an increase of the Yb^{3+} intensity. Close to no emission is observed at the bottom of the film, which is likely due to the low transmission at 980 nm of the film (0.2) as shown in Fig. 4a.

Lastly, the time-resolved intensity of Yb^{3+} (λ_{exc} = 375, λ_{exm} = 980 nm) was measured at the same positions as the transmission and emission measurements and are presented in Fig. 7. The decay of the $^5F_{5/2}$ state of Yb^{3+} is not mono-exponential. The lifetime is, therefore, calculated as a mean lifetime τ_m which is defined as:

Table 2
Position dependent composition, refractive index (n), thickness (d), band-gap (E_{bg}), intensity (I) and mean lifetime τ_{mean} of S1. Measurements are done at white circular markers shown in Fig. 3. Homogenous samples S2, S3 and S4 presented later have a similar Cu/Ga value at Y = 17, 21 and 25 mm respectively.

y (mm)	Cu/Ga	S/(Cu + Ga)	Yb (%)	n	d (nm)	E_{bg} (eV)	I (arb. units)	τ_{mean} (μs)
45 (top)	0.40	1.10	0.6	2.32	940	2.42	0.95	44
41	0.41	1.09	0.4	2.35	890	2.37	1	38
37	0.47	1.08	0.5	2.36	840	2.32	0.85	34
33	0.50	1.08	0.5	2.38	790	2.28	0.68	31
29	0.58	1.07	0.7	2.40	750	2.20	0.57	26
25 (S4)	0.68	1.01	0.7	2.45	690	2.14	0.41	24
21 (S3)	0.81	0.98	0.8	2.53	650	2.09	0.3	20
17 (S2)	0.95	0.93	0.7	2.52	630	2.05	0.08	12
13	1.18	0.90	0.5	–	–	–	0.03	6
9	1.47	0.87	0.6	–	–	–	0.02	3
5 (bottom)	1.91	0.84	0.6	–	–	–	0.004	1

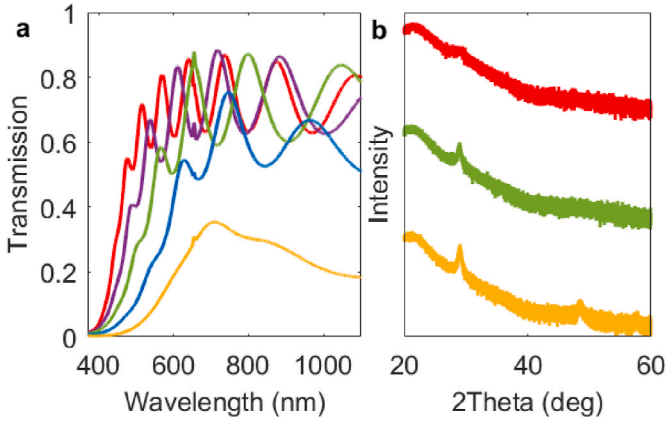

Fig. 4. Transmission spectra (a) and XRD diffractograms (b) of S1 taken at 5 (a) or 3 (b) positions on the film indicated by the colored markers shown in Fig. 3.

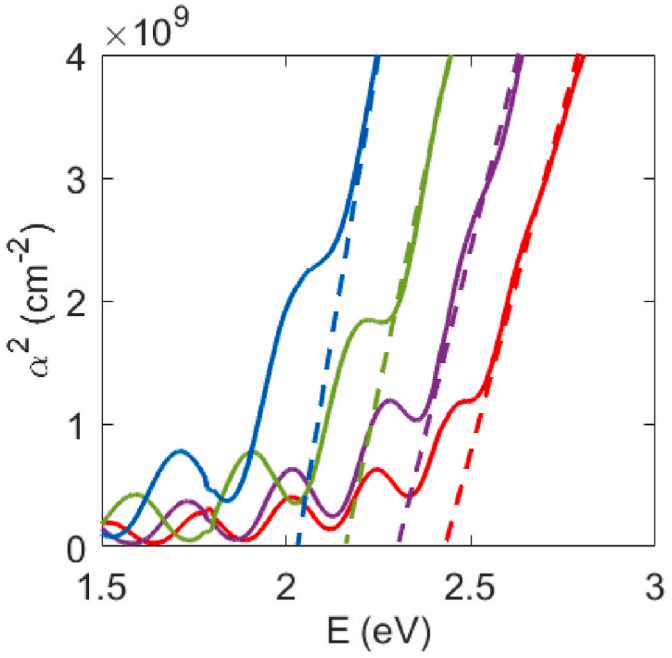

Fig. 5. Tauc plots of S1 at 4 positions on the film indicated by the colored markers shown in Fig. 3.

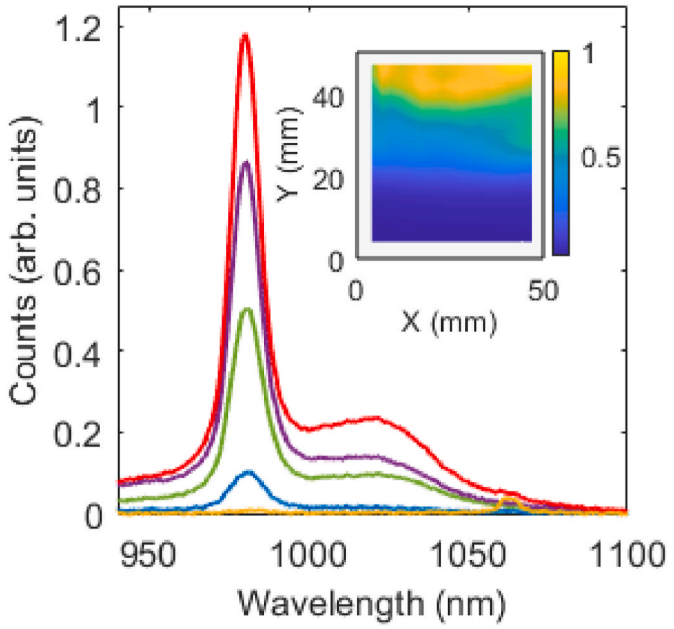

Fig. 6. Emission spectra (λ_{exc} = 375 nm) of S1 taken at the same position as the transmission measurements (Fig. 4) indicated by the corresponding colored markers shown in Fig. 3. The inset shows a heat map of the integrated intensity of the 980 nm Yb^{3+} emission taken at 17x17 positions and interpolated across the film.

$$\tau_m = \frac{\int_0^\infty t^* I_t(t)dt}{\int_0^\infty I_t(t)dt} \quad (4)$$

where t is time after excitation (at t = 0) and $I_t(t)$ is the time-resolved luminescence intensity. The mean lifetime follows a trend similar to the intensity, where the mean lifetime increases from 2 to 37 μs from the bottom to the top of the film. The multi-exponential behavior of the Yb^{3+} decay suggests that a large fraction of the Yb^{3+} ions reside in the amorphous part of our samples causing a wide range of Yb^{3+} ions close to or part of a defect, each with its own non-radiative rate. As will be discussed later in more detail (Fig. 12), it appears that the intrinsic and defect free decay time of Yb^{3+} in $CuGaS_2$ is 110 μs as shown by an exponential tail of the decay common to multiple samples.

The position dependent EDS, transmission, emission and lifetime measurements of S1 demonstrate a trend that Yb^{3+} finds a more suitable site in Cu-poor $CuGaS_2$ films. This is similar to the observed improved $CuInGaSe_2$ solar cell performance in Cu-poor films. The chief reason for

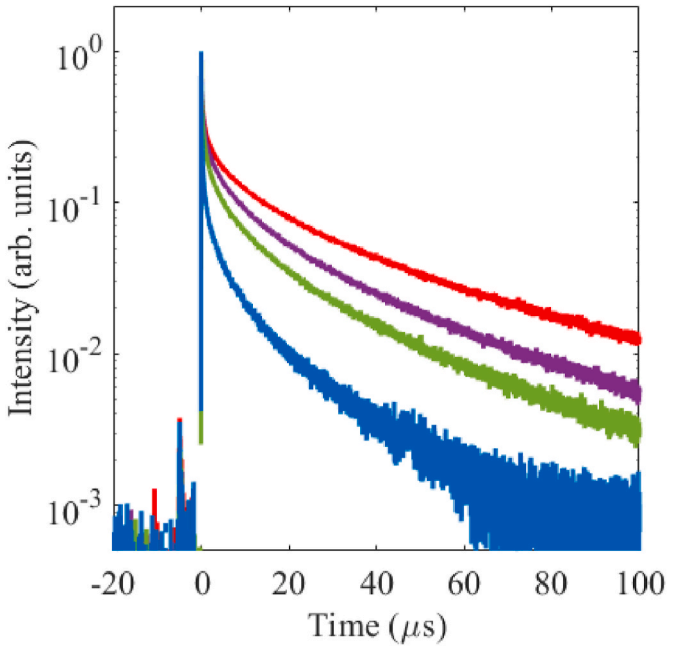

Fig. 7. Time resolved intensity measurements, normalized at t = 0, monitoring 980 nm of S1 taken at 4 positions on the film indicated by the corresponding colored markers in Fig. 3.

improved solar cell efficiency in Cu-poor $CuInGaSe_2$ lies in the suppression of recombination events of the electron-hole pair for two reasons. First, Cu vacancies provide improved hole (the majority charge carrier in CIGS) conductance and second, the valence band maximum is shifted to lower energies [30,31]. These reasons can also play a role for the improved Yb^{3+} intensity as they increase the lifetime and mobility of holes is beneficial for the energy transfer to Yb^{3+} while a lower valence band makes excited Yb^{3+} ions less prone to thermal quenching through the CTS. The role of the VB will be discussed in more detail in relation with the temperature dependent decay measurements. This quenching route becomes less efficient when the valence band is shifted downwards [32]. The data presented above including the composition, refractive index, thickness and estimated band-gap of the film and the intensity and mean decay time of Yb^{3+} along the center vertical are summarized in Table 2.

The position dependent intensity measurements presented in Fig. 6 show that the intensity does not vary significantly across (from left to right) the film. Along the x-direction of the film the Cu, Ga and S content are constant whereas the Yb content varies continuously due to the geometry of the sputter coater as can be seen by the black square markers in Fig. 8. At Y = 17 mm the average Cu:Ga and S:(Cu + Ga) ratios were 0.94:1 and 0.92:1 with a standard deviation of 0.02 and 0.01 respectively. The Yb content decreases linearly from 1.3 to 0.4 % going from the left side to the right side of the sample.

The Yb^{3+} time-resolved intensity was measured (λ_{exc} = 375, λ_{exm} = 980 nm) along the same line as the EDS measurements. The mean lifetime of Yb^{3+} was found to vary between 5.6 and 9.0 μs, with an average of 7.6 μs and a standard deviation of 1.1 μs. The mean lifetime versus X position is shown along the Yb content vs X in Fig. 8. Unlike the Yb content, no trend was observed in the mean lifetime as a function of X position along the Y = 17 mm horizontal. The lack of correlation between the Yb content and mean lifetime indicate that concentration quenching effects play an insignificant role at this range of Yb concentration (0.4–1.3 %, Fig. 8).

In this section we have presented and discussed the nature of Yb^{3+} luminescence in a gradient $CuGaS_2$ film. It is clear that a wider band-gap, Cu-deficient $CuGaS_2$ film is beneficial for the Yb^{3+} efficiency. However, the exact reason for this is still unclear. Temperature

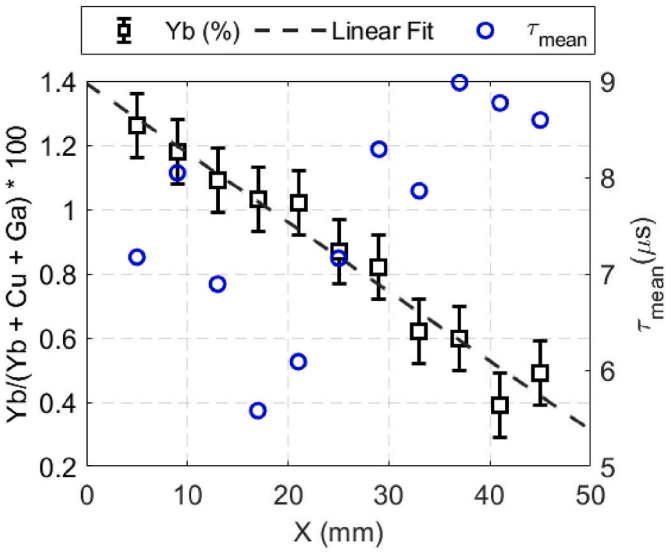

Fig. 8. Position dependent Yb content (black markers, left Y axis) across S1 where the film's composition is closest to stoichiometric $CuGaS_2$ (Y = 17 mm). The black dashed line is a linear fit of the Yb content and x position. Mean radiative lifetime (blue markers, right y axis) of Yb^{3+} at the same positions along Y = 17 mm.

dependent photoluminescence measurements can provide useful data to deepen the understanding of the energy transfer mechanism. To conduct such measurements, it is not feasible to do so on gradient thin films due to experimental limitations. In the next section a comparison is made between four homogenous $CuGaS_2$:Yb films with different Cu:Ga ratios, but a similar thickness and S and Yb content. Temperature dependent lifetime and emission intensity measurements and a low temperature excitation measurement are presented to investigate any thermally activated quenching routes present. Finally, a quantum efficiency measurement at room temperature gives an indication on the energy transfer efficiency of the mechanism presented.

3.2. Homogenous thin films

Four homogenous films, S2, S3, S4 and S4-PA are presented in Fig. 9. The S4-PA sample is a part of the S4 sample which was post annealed (PA) in air for 30 min at 400 °C. EDS measurements are presented in Table 3. The Cu:Ga ratio is 0.95:1, 0.83:1, 0.74:1 and 0.75:1 for S2, S3, S4 and S4-PA respectively. The Yb cation content is approximately 0.3 % for all four samples. The O content in S2, S3 and S4 is around 3.5 %. However, it cannot be excluded that some oxygen EDX signal originated from the substrate. Upon annealing we see that S4-PA has an O content of 14.2 %, while de S content has decreased by roughly the same value, indicating that roughly 20 % of our S is replaced by O after annealing.

Transmission measurements, shown in Fig. 10a, were once again fitted using the Swanepoel method to retrieve the thickness and refractive index. The thickness is found to be 830, 890, 1060 and 1060 nm and the refractive index 2.51, 2.45, 2.40 and 2.38 for S2, S3, S4 and S4-PA respectively. The values for the refractive index follow the same trend as the gradient film, namely a lower Cu:Ga ratio leads to a smaller

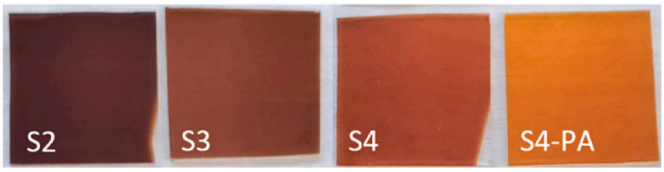

Fig. 9. Photo of the four homogenous samples.

Table 3
Composition of samples S2, S3, S4 and S4-PA given in atomic percentages.

	Cu (%)	Ga (%)	S (%)	O (%)	Yb (%)
S2	23.6	24.4	48.8	3.0	0.2
S3	22.3	26.9	46.7	4.0	0.1
S4	21.0	28.5	46.7	3.7	0.1
S4-PA	20.6	27.5	37.6	14.2	0.1

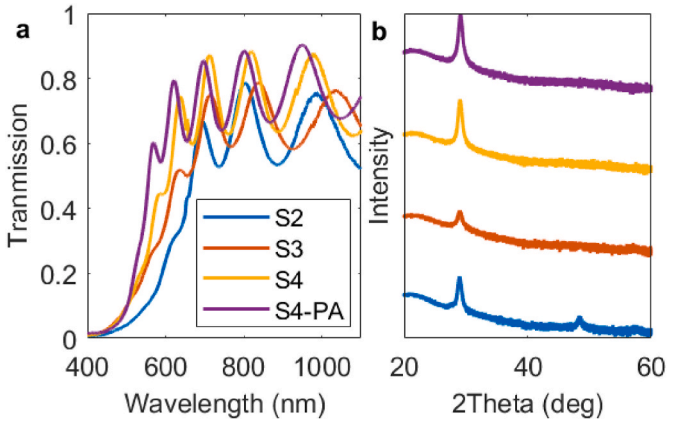

Fig. 10. Transmission (a) and XRD (b) measurements of S2, S3, S4 and S4 – PA.

refractive index. The annealing of S4 in oxygen resulted in a slightly lower refractive index as some sulphur is replaced by oxygen. For samples S2 and S3 we note that the maxima of the interference fringes decreases at longer wavelengths, whereas for S4 and S4-PA this is not the case. The key interest for this work is the slight shifting of the absorption edge between the four samples and how this affects the Yb^{3+} luminescence. It can be concluded that the properties of the homogeneous films are largely identical to the indicated locations at the gradient film as intended.

XRD measurements showed characteristic $CuGaS_2$ peaks. Results are shown in Fig. 10b. Once again a single peak is observed at 28°, like in the gradient film. We note that the Cu-rich film, S2, has a second peak at 48° which is not present in the other measurements, despite S4 and S4-PA having a higher peak intensity at 28°. This can be due to S2 being less textured and having more random orientations, rather than one single orientation. Similar to the gradient films, other phases such as Cu, CuS, CuS_2, CuO, Cu_2O or Ga_2S_3 were not observed. The post annealing of S4 did not significantly improve the crystallinity in terms of observed intensity. There is a slight shift in the peak of 0.1° to the right, likely due to the incorporation of the smaller O ion in the lattice. Previous work has shown a CuO phase developing after post annealing $CuGaS_2$ thin films for 2 h at 400 °C [33]. We do not find such a phase present in our sample.

Emission (λ_{exc} = 375 nm) of the four samples is shown in Fig. 11. We can see that luminescence intensity is increased substantially from S2 to S4 – PA. Between S2 and S4 the intensity is improved by roughly 25 times. We do not observe this significant increase in intensity within the gradient film (between Y = 17 and 25 mm). After post annealing S4, the intensity is further increased by factor a of 15. These results show that Yb^{3+} luminescence is strongly affected by the Cu:Ga ratio and the incorporation of O. A shift of the peak intensity of Yb^{3+} between S3 and S4 of about 1.5 nm is observed, indicating that the site at which Yb^{3+} is located is affected by the Cu:Ga ratio.

Temperature dependent lifetime measurements at (λ_{exc} = 375, λ_{exm} = 980 nm) are shown in Fig. 12a–d. The same intensity- and time scale are chosen on the axis to be able to compare the shape of the decay curves between the samples. The same number of laser pulses were used at each temperature and the decay curves are plotted as measured and not normalized to unity. The intensity differences at t = 0 between samples is cause mainly by alignment differences between laser, sample

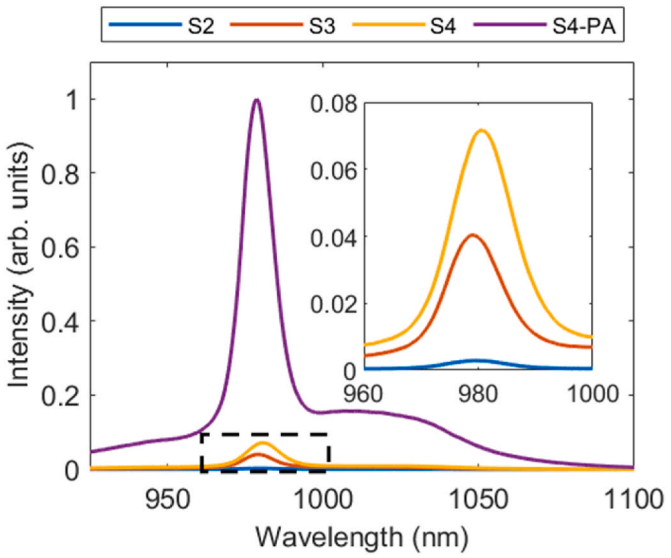

Fig. 11. Emission intensity of Yb^{3+} (λ_{exc} = 375) of S2, S3, S4 and S4 – PA at room temperature.

and detector. That is why S2 show a relatively poor intensity. For comparing intensities between samples Fig. 11 should be used. The tail of the emission for S3, S4 and S4-PA can reasonably well be approximated with a single exponential with a decay time of 110 μs, as shown by the dashed black lines, that does not change with temperature. Yb^{3+} lifetime in sulfides ranges between 1.2 ns up to 400 μs in MoS_2:Yb^{3+} and $PbIn_2S_4$:Yb^{3+} respectively [34,35]. While in CdSe:Yb3+ quantum dots exhibit a Yb^{3+} lifetime up to 160 μs [10]. The observed lifetime of 110 μs in our $CuGaS_2$:Yb^{3+} thin film fits within this range, though relatively short. No literature data is found on Yb^{3+} lifetime in materials with a chalcopyrite structure. The variation in Yb^{3+} lifetime in chalcogenides is influenced by composition, crystallinity and structure and therefore a comparison of Yb^{3+} lifetime is difficult to do between compounds. The lowering of the integrated intensity towards higher temperature is due to an increasingly larger contribution of a fast non-exponential component. Although our samples show a complex non-exponential behavior, it is possible to derive a number of conclusions from a qualitative analysis. For this we discriminate between two different situations: the first is a classical situation in which the decay curves become steeper toward higher temperature due to a temperature dependent quenching of excited Yb^{3+} ions. In such a situation decay curves have a constant intensity at t = 0. In a second situation, excited Yb^{3+} ions have no temperature-dependent quenching but rather a temperature dependent host-to-Yb^{3+} energy transfer. In that case decay curves have a constant slope but the intensity at t = 0 decreases towards higher temperature. In both cases an energy barrier ΔE controls the temperature dependence. The constant slope of the decay tails of all our samples suggest the second situation is predominantly active. As indicated by the two parallel dashed lines in each graph for S3, S4 and S4-PA, the slope of the tail of the decay curves does not change significantly with temperature and remains about 110 μs for the three samples. This decay time is therefore interpreted as the intrinsic decay time of Yb^{3+} in this sulfide host without any defects.

No exciton emission from the host is observed at 77 K, unlike other reports in $CuGaS_2$ crystals [36]. The lack of exciton emission suggests that there is an efficient and fast non-radiative recombination of the hole and electron after excitation. A low lifetime of electron-hole pairs would be detrimental to the energy transfer mechanism.

We also note the presence of slower decaying Yb^{3+} ions present in the S4-PA sample. Temperatures below room temperature show a clear slow decaying component with a lifetime of approximately 1.4 ms, indicated again by a dashed black line shown in Fig. 13. This decay time is similar

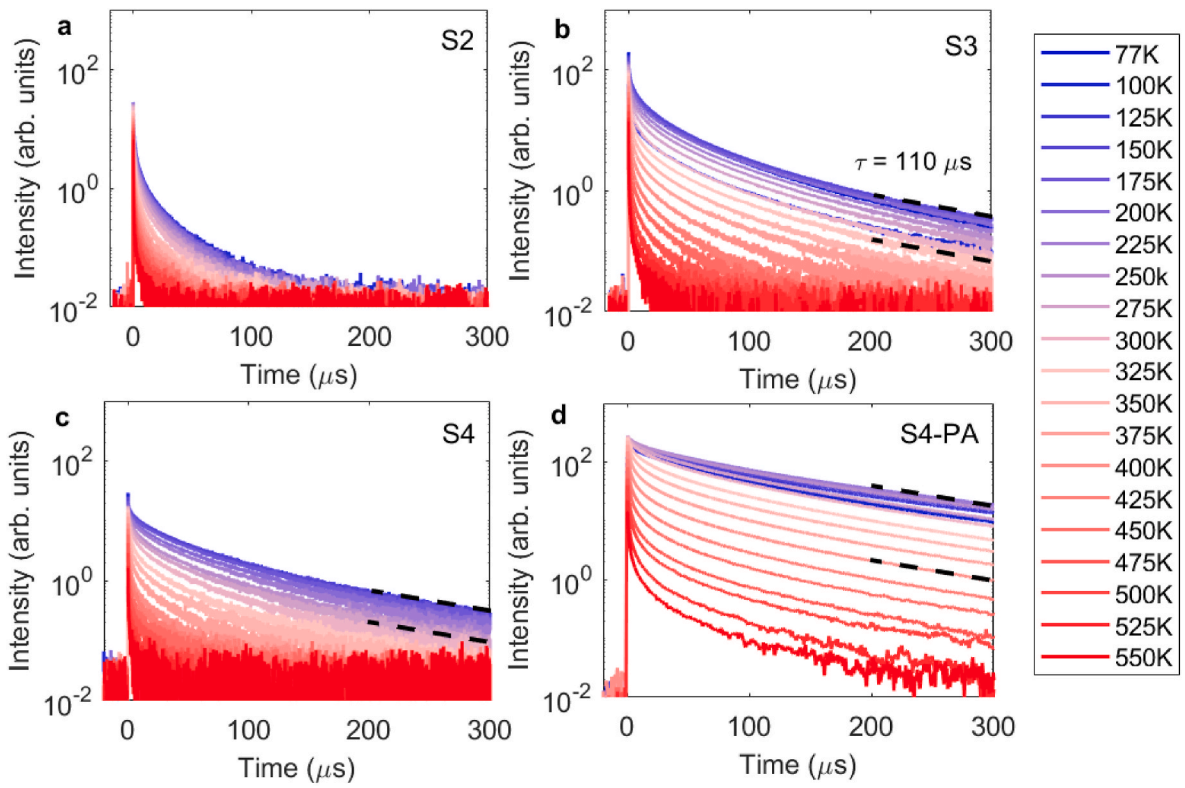

Fig. 12. Temperature dependent (77–550 K) time resolved Yb^{3+} emission (λ_{exc} = 375, λ_{exm} = 980 nm) of S2, S3, S4 and S4-PA shown in (a), (b), (c) and (d) respectively. The arrow in (a) is shown to indicate increasing temperature and has been omitted in (b), (c), and (d) for clarity. The tail of the emission is fitted with a single exponential in (b), (c) and (d) indicated by the black dashed line.

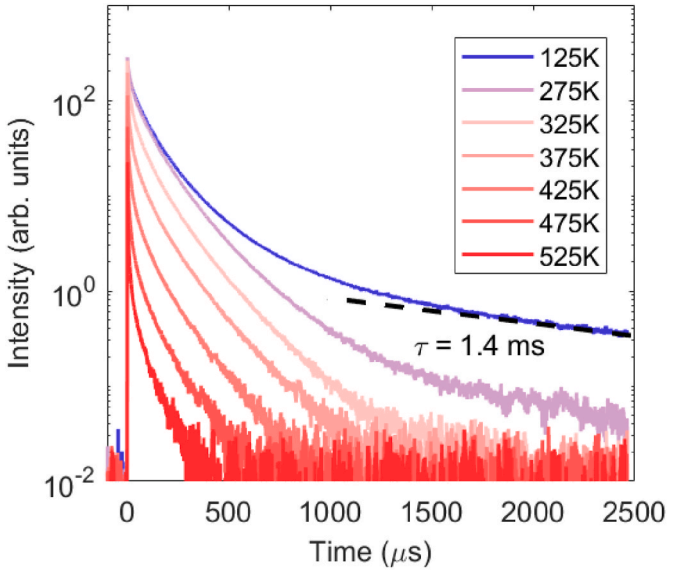

Fig. 13. Temperature dependent time resolved intensity of Yb^3 (λ_{exc} = 375, λ_{exm} = 980 nm) in S4-PA. The tail of the emission at 125 K is fitted with a single exponential indicated by the black dashed line.

to Yb^{3+} ions found in oxide materials [37]. The significantly longer lasting decay component does not explain the higher emission intensity of S4-PA as the intensity has already dropped by two orders of magnitude by the time the slow component becomes visible, thereby not contributing significantly towards the overall emission intensity. Rather the annealing is likely to improve the energy transfer efficiency by reducing defects in the host material and with that increase the emission intensity.

The temperature dependent intensity of Yb^{3+} for S2, S3, S4 and S4-PA is found by integrating the time-resolved emission intensity in Fig. 12. To find an activation energy related to the observed thermal quenching, an Arrhenius plot is made. The Arrhenius equation is defined as follows:

$$I_{(T)} = \frac{I_0}{1 + A^* e^{-\frac{\Delta E}{kT}}} \quad (5)$$

Where A is a pre-exponential factor, ΔE is the activation energy, k the Boltzmann constant, T the temperature and I_0 the intensity at T = 77 K. Based on this equation one can plot $\ln(I_0/I_T - 1)$ vs 1/kT and obtain a linear relationship where the slope is equal to the activation energy. Two such plots, with linear fits, for S2 and S4-PA are shown in Fig. 14, the others are omitted for clarity. The activation energies for S2, S3, S4 and S4-PA are found to be 0.15, 0.22, 0.20 and 0.28 eV respectively. As mentioned before, the temperature quenching appears to be due to a reduction in the number of Yb^{3+} ions that get excited after transfer from the host lattice. In the proposed energy transfer mechanism, reviewed in the introduction, the first step to excite Yb^{3+} is by trapping the electron in the Yb^{2+} ground state. The de-trapping of the electron is thermally activated and would result in less excited Yb^{3+} ions and thereby a lower intensity. The activation energy found using the Arrhenius plot therefore represents the energy difference between the Yb^{2+} ground state and the bottom of the conduction band better known as the electron trap depth. A more detailed analysis of especially the fast component is beyond the scope of this work because the intensity at t = 0 is prone to experimental error due to the limited temporal resolution (bin size) of 1 ns of our measurements which determines the intensity at t = 0.

The Yb^{2+} ground state generally resides at −3.5 eV on the vacuum referred binding energy scale which suggests that the conduction band lies around −3.3 eV which is very similar to previously measured values

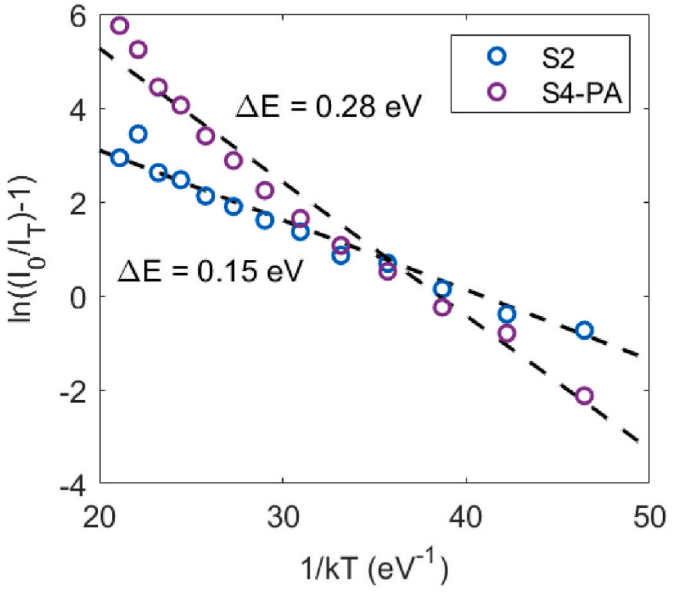

Fig. 14. Arrhenius plot showing the emission intensity plotted against 1/kT for S2, S3, S4 and S4-PA. The black dashed line is a fit using the Arrhenius equation (5).

based on electrochemical techniques studies [38,39]. For LSC application considerations, a larger trap depth would avoid significant thermal quenching at room temperature. This could be the case for $CuAlS_2$ that is known to have a higher energy CB. In our most efficient sample, S4-PA, we find that at room temperature the intensity is lower by a factor of 0.56 compared to at 77K.

Lastly, we present the transmission, excitation and emission spectra of our most optimal sample, S4 – PA, in a single plot (Fig. 15). It is expected that the excitation spectra consists of two main features. First is the excitation through the proposed mechanism which involves the creation of an electron-hole pair in the host (band-gap excitation) and the other would be a direct excitation of Yb^{3+} through a charge transfer transition. The excitation spectrum we present has numerous features which makes it difficult to interpret. We note a peak (split in two) around 483 nm, or 2.57 eV. This peak corresponds to the start of the

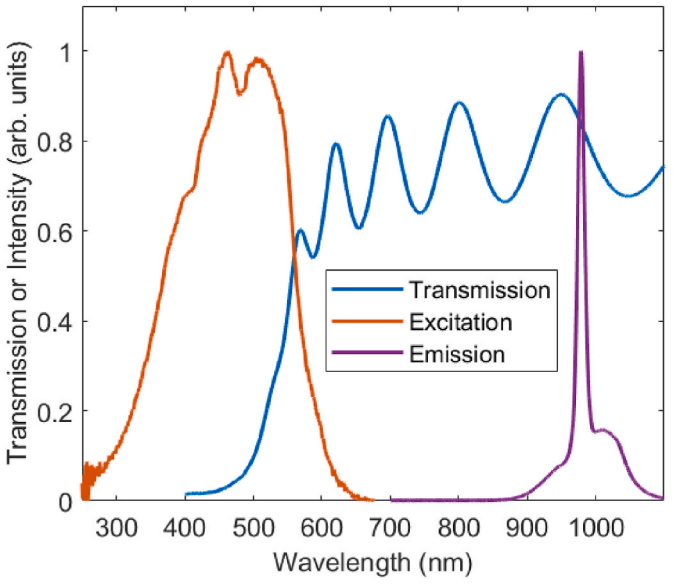

Fig. 15. Excitation and emission spectra ($\lambda_{exc} = 375$, $\lambda_{exm} = 980$ nm) of S4 – PA at 77K. Transmission measurement taken at room temperature.

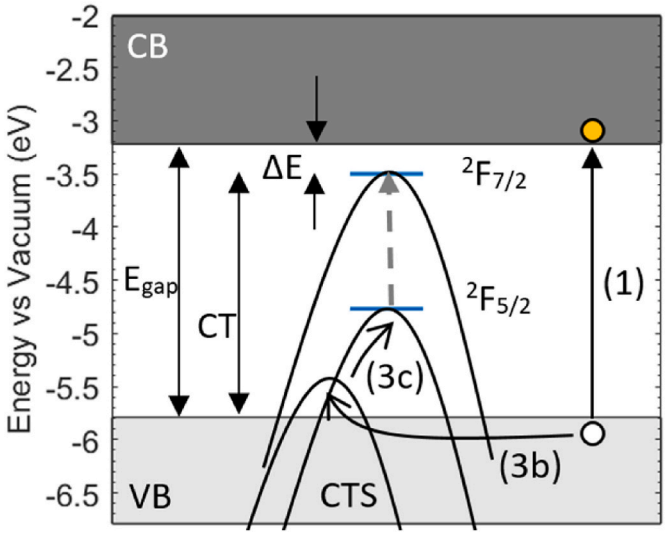

Fig. 16. Proposed VRBE diagram of $CuGaS_2$:Yb^{3+} (S4-PA) using the values for the activation energy (ΔE) for luminescence quenching and the band-gap (E_{gap}) found experimentally. Parabola's are placed in the context of the 'hole picture discussed in the introduction'.

absorption edge shown by the transmission spectra indicating that this is the band-gap. 2.57 eV is a slightly higher energy than the reported band-gap of 2.43 eV for $CuGaS_2$ [40]. However a larger band-gap is expected for S4-PA as it is deficient in Cu and post annealed in air. Using the 0.28 eV electron trap depth found earlier, we can estimate that the charge transfer energy (i.e. the distance between the valence band and Yb^{2+} ground state) is 2.57–0.28 = 2.29 eV, or 541 nm. Again, due to the numerous broad peaks present in the measurement it is unclear if we truly observe the charge transfer transition. The quantum efficiency (QE) of S4 – PA was found to be of the order of 0.01 % when excited by a 375 nm LED with a full width at half maxima of 25 nm. It was not feasible to measure the QE of the other samples as they were simply too dim.

Taking the activation energy, ΔE, found from the Arrhenius plot along with the suggested band-gap, E_{gap}, found from the excitation and transmission measurements we can construct a VRBE scheme as shown in Fig. 16. The route of the hole is depicted once again to show the energy transfer mechanism as discussed in the introduction.

4. Conclusion

It has been shown, using a gradient sputtering method, that the widening of the band-gap of $CuGaS_2$ towards a larger Cu-deficiency, increases the Yb^{3+} emission intensity by 25 fold. This was explained by an more efficient hole transport (to Yb^{2+}), a well-known effect in $CuInGaSe_2$ solar cells [30]. Post-annealing in air did not increase the crystallinity but resulted in a 15 times higher intensity most likely related to incorporation of 15 % O ions.

The role played by oxygen needs to be investigated further. Temperature dependent decay curves of Yb^{3+} emission indicate a single energy barrier varying between 0.15 and 0.28 eV depending on composition, that is interpreted as the energy of the Yb^{2+} ground state below the conduction band. The thermal release of trapped electrons causes the intensity at room temperature to be 0.56 times lower than without thermal quenching at 77K. The unexpectedly low IQE of 0.01 % must however be explained by a more severe quenching process involving many non-radiative decay pathways of the generated electron-hole pairs due to the non-stoichiometric defective amorphous nature of the films. Just 1 in 10.000 electrons are trapped by Yb^{3+}. It is concluded that the energy transfer is due to electron trapping, followed by hole-trapping. After hole trapping, excited Yb^{3+} ions show no further

quenching evidenced by a temperature independent decay tail of 110 μs. Although the strong and UV-VIS absorber characteristics of $CuGaS_2$ are favourable for LSC application, the poor energy transfer to Yb^{3+} is obviously not. The temperature dependent quenching at room temperature can be mitigated by for example replacing Ga with Al, lifting the CB [41]. It remains to be seen whether increasing the quality of the films can lower the electron-hole non-radiative recombination sufficiently. Overall, it can be concluded that the tune-ability of Cu(Al,Ga,In) (S,Se,Te)$_2$ along with the gradient thin film approach allows for fascinating research into the nature of the energy transfer mechanisms from the host to lanthanide or transition metal ions.

CRediT authorship contribution statement

Max Derksen: Writing – review & editing, Writing – original draft, Visualization, Supervision, Investigation, Data curation, Conceptualization. **Sem Bergkamp:** Writing – review & editing, Validation, Methodology, Investigation. **Olivia Kohnstamm:** Writing – review & editing, Validation, Methodology, Investigation, Conceptualization. **Erik van der Kolk:** Writing – review & editing, Supervision, Project administration, Investigation, Funding acquisition, Formal analysis, Conceptualization.

Declaration of competing interest

The authors declare that they have no known competing financial interests or personal relationships that could have appeared to influence the work reported in this paper.

Data availability

Data will be made available on request.

Acknowledgments

This work was supported by the Netherlands Organization for Scientific Research (NWO), as part of the High-Tech Systems and Materials (HTSM) program with project number NWO:17105.

References

[1] L.L. Kazmerski, F.R. White, G.K. Morgan, Thin-film CuInSe2/CdS heterojunction solar cells, Appl. Phys. Lett. 29 (4) (1976) 268–270, https://doi.org/10.1063/1.89041.
[2] J. Gifford, Solar Frontier hits 22.3% on CIGS cell, PV Magazine 12 (08) (2015), 1-1, https://www.pv-magazine.com/2015/12/08/solar-frontier-hits-22-3-on-cigs-cell_100022342/.
[3] T.D. Lee, A.U. Ebong, A review of thin film solar cell technologies and challenges, Renew. Sustain. Energy Rev. 70 (2017) 1286–1297, https://doi.org/10.1016/j.rser.2016.12.028.
[4] W.H. Weber, J. Lambe, Luminescent greenhouse collector for solar radiation, Appl. Opt. 15 (10) (1976/10/01 1976) 2299–2300, https://doi.org/10.1364/AO.15.002299.
[5] M. Rafiee, S. Chandra, H. Ahmed, S.J. McCormack, An overview of various configurations of Luminescent Solar Concentrators for photovoltaic applications, Opt. Mater. 91 (2019) 212–227, https://doi.org/10.1016/j.optmat.2019.01.007.
[6] B.C. Rowan, L.R. Wilson, B.S. Richards, Advanced material concepts for luminescent solar concentrators, IEEE J. Sel. Top. Quant. Electron. 14 (5) (2008) 1312–1322, https://doi.org/10.1109/jstqe.2008.920282.
[7] H. Li, et al., Engineering CIGS grains qualities to achieve high efficiency in ultrathin Cu(InxGa1−x)Se2 solar cells with a single-gradient band gap profile, Results Phys. 12 (2019) 704–711, https://doi.org/10.1016/j.rinp.2018.12.043.
[8] D.A. Chengelis, A.M. Yingling, P.D. Badger, C.M. Shade, S. Petoud, Incorporating lanthanide cations with cadmium selenide nanocrystals: a strategy to sensitize and protect Tb(III), J. Am. Chem. Soc. 127 (48) (2005/12/01 2005) 16752–16753, https://doi.org/10.1021/ja0511725.
[9] W. Luo, R. Li, X. Chen, Host-sensitized luminescence of Nd3+ and Sm3+ ions incorporated in anatase titania nanocrystals, J. Phys. Chem. C 113 (20) (2009/05/21 2009) 8772–8777, https://doi.org/10.1021/jp901862k.
[10] R. Martin-Rodriguez, R. Geitenbeek, A. Meijerink, Incorporation and luminescence of Yb3+ in CdSe nanocrystals, J. Am. Chem. Soc. 135 (37) (Sep 18 2013) 13668–13671, https://doi.org/10.1021/ja4077414.
[11] T. Förster, Zwischenmolekulare Energiewanderung und Fluoreszenz, Ann. Phys. 437 (1–2) (1948) 55–75, https://doi.org/10.1002/andp.19484370105.
[12] D.L. Dexter, A theory of sensitized luminescence in solids, J. Chem. Phys. 21 (5) (1953) 836–850, https://doi.org/10.1063/1.1699044.
[13] P. Mukherjee, C.M. Shade, A.M. Yingling, D.N. Lamont, D.H. Waldeck, S. Petoud, Lanthanide sensitization in II-VI semiconductor materials: a case study with terbium(III) and europium(III) in zinc sulfide nanoparticles, J. Phys. Chem. A 115 (16) (Apr 28 2011) 4031–4041, https://doi.org/10.1021/jp109786w.
[14] G.H. Debnath, S. Rudra, A. Bhattacharyya, N. Guchhait, P. Mukherjee, Host sensitized lanthanide photoluminescence from post-synthetically modified semiconductor nanoparticles depends on reactant identity, J. Colloid Interface Sci. 540 (Mar 22 2019) 448–465, https://doi.org/10.1016/j.jcis.2019.01.034.
[15] G.H. Debnath, P. Mukherjee, D.H. Waldeck, Optimizing the key variables to generate host sensitized lanthanide doped semiconductor nanoparticle luminophores, J. Phys. Chem. C 124 (49) (2020) 26495–26517, https://doi.org/10.1021/acs.jpcc.0c07548.
[16] P. Dorenbos, Systematic behaviour in trivalent lanthanide charge transfer energies, J. Phys. Condens. Matter 15 (49) (2003) 8417.
[17] P. Dorenbos, Locating lanthanide impurity levels in the forbidden band of host crystals, J. Lumin. 108 (1–4) (2004) 301–305.
[18] P. Dorenbos, The Eu3+ charge transfer energy and the relation with the band gap of compounds, J. Lumin. 111 (1) (2005/01/01/2005) 89–104, https://doi.org/10.1016/j.jlumin.2004.07.003.
[19] P. Dorenbos, E. van der Kolk, Location of lanthanide impurity levels in the III-V semiconductor GaN, Appl. Phys. Lett. 89 (6) (2006), https://doi.org/10.1063/1.2336716.
[20] P. Dorenbos, E. van der Kolk, Location of lanthanide impurity energy levels in the III–V semiconductor AlxGa1−xN (0⩽x⩽1), Opt. Mater. 30 (7) (2008/03/01/2008) 1052–1057, https://doi.org/10.1016/j.optmat.2007.05.019.
[21] P. Dorenbos, Lanthanide charge transfer energies and related luminescence, charge carrier trapping, and redox phenomena, J. Alloys Compd. 488 (2) (2009/12/04/2009) 568–573, https://doi.org/10.1016/j.jallcom.2008.09.059.
[22] P. Dorenbos, The hole picture as alternative for the common electron picture to describe hole trapping and luminescence quenching, J. Lumin. 197 (2018) 62–65, https://doi.org/10.1016/j.jlumin.2018.01.013.
[23] R. Heitz, et al., Excited states of Fe 3+ in GaN, Phys. Rev. B 55 (7) (1997) 4382.
[24] C. Guillén, J. Herrero, CuInS2 and CuGaS2 thin films grown by modulated flux deposition with various Cu contents, Phys. Status Solidi 203 (10) (2006) 2438–2443, https://doi.org/10.1002/pssa.200622132.
[25] S.M. Kong, R. Fan, S.H. Jung, C.W. Chung, Characterization of Cu(In,Ga)Se2 thin films prepared by RF magnetron sputtering using a single target without selenization, J. Ind. Eng. Chem. 19 (4) (2013/07/25/2013) 1320–1324, https://doi.org/10.1016/j.jiec.2012.12.035.
[26] W.-J. Jeong, G.-C. Park, Structural and electrical properties of CuGaS2 thin films by electron beam evaporation, Sol. Energy Mater. Sol. Cell. 75 (1) (2003/01/01/2003) 93–100, https://doi.org/10.1016/S0927-0248(02)00110-1.
[27] E.P.J. Merkx, E. van der Kolk, Method for the detailed characterization of cosputtered inorganic luminescent material libraries, ACS Comb. Sci. 20 (11) (2018/11/12 2018) 595–601, https://doi.org/10.1021/acscombsci.8b00068.
[28] R. Swanepoel, Determination of the thickness and optical constants of amorphous silicon, J. Phys. E Sci. Instrum. 16 (12) (1983/12/01 1983) 1214, https://doi.org/10.1088/0022-3735/16/12/023.
[29] J. Tauc, Optical properties and electronic structure of amorphous Ge and Si, Mater. Res. Bull. 3 (1) (1968) 37–46.
[30] T. Nishimura, K. Nakada, A. Yamada, Examination of a Cu-deficient layer on Cu(In,Ga)Se2 films fabricated by a three-stage process for highly efficient solar cells, ACS Appl. Energy Mater. 2 (7) (2019/07/22 2019) 5103–5108, https://doi.org/10.1021/acsaem.9b00774.
[31] T. Maeda, W. Gong, T. Wada, Crystallographic and optical properties and band structures of CuInSe 2 , CuIn 3 Se 5 , and CuIn 5 Se 8 phases in Cu-poor Cu 2 Se–In 2 Se 3 pseudo-binary system, Jpn. J. Appl. Phys. 55 (2016), https://doi.org/10.7567/JJAP.55.04ES15.
[32] P. Dorenbos, Thermal quenching of lanthanide luminescence via charge transfer states in inorganic materials, J. Mater. Chem. C (2023).
[33] F. Smaïli, M. Kanzari, Effect of oxygen on the surface morphology of CuGaS2 thin films, Mater. Sci. Eng. C 29 (6) (2009/08/01/2009) 1969–1973, https://doi.org/10.1016/j.msec.2009.03.013.
[34] S.E. Creutz, R. Fainblat, Y. Kim, M.C. De Siena, D.R. Gamelin, A selective cation exchange strategy for the synthesis of colloidal Yb3+-doped chalcogenide nanocrystals with strong broadband visible absorption and long-lived near-infrared emission, J. Am. Chem. Soc. 139 (34) (2017) 11814–11824.
[35] C. Maddi, et al., Structural, spectroscopic, and excitonic dynamic characterization in atomically thin Yb3+-doped MoS2, fabricated by femtosecond pulsed laser deposition, Adv. Opt. Mater. 7 (21) (2019) 1900753.
[36] S. Shirakata, K. Saiki, S. Isomura, Excitonic photoluminescence in CuGaS2 crystals, J. Appl. Phys. 68 (1) (1990) 291–297, https://doi.org/10.1063/1.347131.
[37] Q.H. Yang, J. Ding, H.W. Zhang, J. Xu, Investigation of the spectroscopic properties of Yb3+-doped yttrium lanthanum oxide transparent ceramic, Opt Commun. 273

(1) (2007/05/01/2007) 238–241, https://doi.org/10.1016/j.optcom.2006.12.035.
[38] C. Li, J. He, Y. Xiao, Y. Li, J.-J. Delaunay, Earth-abundant Cu-based metal oxide photocathodes for photoelectrochemical water splitting, Energy Environ. Sci. 13 (10) (2020) 3269–3306.
[39] P. Dorenbos, [INVITED] Improved parameters for the lanthanide 4f and 4f−5d curves in HRBE and VRBE schemes that takes the nephelauxetic effect into account, J. Lumin. 222 (2020/06/01/2020) 117164, https://doi.org/10.1016/j.jlumin.2020.117164.
[40] J. Shay, P. Bridenbaugh, H. Kasper, Luminescent properties of CuGaS2 doped with Cd or Zn, J. Appl. Phys. 45 (10) (1974) 4491–4494.
[41] M. Caglar, S. Ilican, Y. Caglar, Structural, morphological and optical properties of CuAlS2 films deposited by spray pyrolysis method, Opt Commun. 281 (6) (2008) 1615–1624.